In situ conversion of artificial proton-rich shell to inorganic maskant toward stable single-crystal Ni-rich cathode

Haoyu Xue[a‡], Yongzhi Liang[a‡], Yuxiang Huang[b], Yuchen Ji[a], Zhongxing Xu[a], Xinhan Chen[c], Honghao Wang[d], Jiajie Liu[a], Khalil Amine[f], Tongchao Liu[f]*, Xinghua Tan[a,e]*, Feng Pan[a]*

[a]School of Advanced Materials, Peking University Shenzhen Graduate School, Shenzhen, 518055, China

[b]Department of Chemistry, The University of Hong Kong, Hong Kong, 999077, China

[c]School of Materials, Sun Yat-sen University, Shenzhen, China. 518107

[d]School of Science and Engineering, The Chinese University of Hong Kong, Shenzhen 518172, China.

[e]Shenyang National Laboratory for Materials Science, Institute of Metal Research, Chinese Academy of Sciences, Shenyang 110016, China.

[f]Chemical Sciences and Engineering Division, Argonne National Laboratory, Lemont, IL, 60439 USA

‡These authors contributed equally to this work.

*Corresponding authors: liut@anl.gov (T.L.), xhtan@imr.ac.cn (X.T.), panfeng@pkusz.edu.cn (F.P.)

Key words: proton; electrochemical conversion; LiF and Li_3PO_4 sub-nano particle; dense maskant; nickel-rich single crystal;

Abstract

Single-crystal high-nickel oxide with an integral structure can prevent intergranular cracks and the associated detrimental reactions. Yet, its low surface-to-volume ratio makes surficial degradation a more critical factor in electrochemical performance. Herein, artificial proton-rich (ammonium bicarbonate) shell was successfully introduced on the nickel-rich $LiNi_{0.92}Co_{0.06}Mn_{0.02}O_2$ single crystals for in situ electrochemically conversing into inorganic maskant to enhance stability of cathode. The process is that the surficial enriched proton, once released from the ammonium bicarbonate shell (proton reservoir) during 1st charge, was immediately captured by $LiPF_6$, in situ electrochemically conversing to LiF and Li_3PO_4 sub-nano particle dense maskant (sub-nano F-&P-maskant). The in situ formed compact nano F-&P-maskant significantly resists the cathode against electrolyte attack and improves the surface stability of particles during long-term cycling. Consequently, this surface modification enables 95% capacity retention after 100 cycles at a high voltage of 4.5 V in the half cell and 83% capacity retention after 800 cycles in the full cell. This work demonstrates a strategy for reconstructing the protective layer using the rational design of surficial enriched proton shells for advanced lithium batteries.

Introduction

Lithium-ion batteries with high energy density and durable cyclability have become a key focus to meet the rapidly growing demands of electric vehicles. Among the current state-of-the-art cathodes, $LiNi_xCo_yMn_{1-x-y}O_2$ (NCM) with nickel content exceeding 90% has emerged as a promising candidate cathode for the next generation of high energy batteries[1]. However, severe electrochemical degradation driven by surface reaction[2], structure degradation[3] and lattice strain at high-delithiation states continues to impede their widespread commercialization. Additionally, conventional poly-crystalline Ni-rich cathodes suffer from intergranular and intragranular cracks due to the anisotropic volume change, particularly abrupt contractions at high delithiation states[4], which unavoidably exposes more reactive surfaces and exacerbates the issues aforementioned, leading to rapid capacity degradation. In contrast, single crystalline cathodes with enhanced morphological integrity eliminate intergranular cracks and enhance morphological integrity.[5] Whereas, surface parasitic reactions, though reduced in single crystal cathode, are still unavoidable. Unlike polycrystalline cathodes where Li ions can move through both grain boundaries and lattice, in single crystal cathodes, Li ion transport from the bulk of single crystal to electrolyte must occur through their surface, which make the surficial degradation a more critical factor for their performance. This underscores the need for effective strategies to improve the surface tolerance and stability of single crystal cathodes.

Surface coating is one of the most effective approaches to alleviate the surficial side

reaction between electrolyte and cathode[6]. And, the structure configuration of the coating layer, including the constituent, thickness and uniformity, dominates the effect of Li^+ transport properties (such as ionic conductivity and diffusion homogeneity) and long-term surface stability[7]. However, conventional coating engineering with uneven distribution proves difficult to meet with the multiple requirements mentioned above, which as a result restrict the effects in capacity delivering[8] and long-term cycling[9]. Recently, parallel research in our group have found that the part conversion of the coating layer during electrochemical cycling can form improved reconstructed interlayer beyond the original one[10]. Yet, in situ full transformation of the coating layer and the related optimization mechanism for the corresponding reconstructed layer in enhancing cycle performance is rarely reported.

Proton, proved by previous researches[11], can react with the $LiPF_6$ to generate LiF and Li_3PO_4. The LiF- and and Li_3PO_4- involved artificial covering have been realized ideal maskants due to their strong mechanical strength, super chemical stability, and low Li^+ diffusion barrier[7, 12]. Hence, the F- and P-based maskant formation can be potentially driven by the proton as well. Whereas, the positive discussion of proton utilization and the correlative F- and P-based maskant is rare. One of the main reasons is that it is hard to automatically formation of the compact inorganics-rich surface layer on the electrode by the well-distributed trace proton in the electrolyte. This underscores the potential strategies to controllably introduce locally high-concentration protons on the cathode surface to form

a compact F- and P-based maskant.

In this work, by adopting an artificially uniform ammonium bicarbonate shell as proton-reservoir on the single crystal nickel-rich cathode $LiNi_{0.92}Co_{0.06}Mn_{0.02}O_2$ (SN92-H), we demonstrate that the surficial enriched proton can *in-situ* converted into LiF and Li_3PO_4 sub-nano particle dense maskant in combination with $LiPF_6$ during the first electrochemical cycle. Illustrated by the comprehensive characterization of operando Fourier-transform infrared spectroscopy (FT-IR), in situ ultraviolet-visible spectroscopy (UV), Time-of-Flight Secondary Ion Mass Spectrometry (ToF-SIMs) and Cryogenic transmission electron microscopy (cryo-TEM), the in situ conversion of the proton-enriched shell to sub-nano F-&P-maskant was systematically revealed. The resulting compact sub-nano F-&P-dense maskant is effective in defending the cathode particle from the attack of electrolyte and suppressing the correlated lattice oxygen loss and transition metal dissolution. As a result, the SN92-H exhibits significantly improved electrochemical performance, with 95% capacity retention after 100 cycles within the voltage range of 2.75-4.5 V in half cells, and notably excellent capacity retention of 83% after 800 cycles in full cells. This article highlights an inspiring route of coating layer in situ reconstruction and provides a comprehensive understanding of the protons in forming the LiF and Li_3PO_4 sub-nano particle dense maskant.

Result and Discussion

Construction of artificial proton-rich shell

The proton reservoir, ammonium bicarbonate, was uniformly deposited on the commercial single crystals nickel-rich $LiNi_{0.92}Co_{0.06}Mn_{0.02}O_2$ (SN92, the morphology and surface structure are shown in **Fig. S1-2** and the element ratio is displayed in **Table. S1**) via sealed tube heating method. As characterized by high-resolution TEM (**Fig. 1a**), there was a 5~7 nm amorphous layer on the surface of the SN92-H particle after the low temperature annealing of the mixture (SN92 and ammonium bicarbonate). To clearly figure out the reaction route and composition of the amorphous layer, energy dispersive spectrometer (EDS) and X-ray photoelectron spectroscopy (XPS) were conducted. According to the TEM-EDS (**Fig. 1b**) and SEM-EDS (**Fig. S3**) images, apart from the inherent transition metal element of Ni, Co and Mn, N and C elements also uniformly distribute on the SN92-H particles, demonstrating that the amorphous layer containing N and C elements. In sharp contrast, the SN92 shows negligible N and C elements (**Fig. S4**). The further XPS test proved the presence of NH_4^+ and CO_3^{2-} on the surface of SN92-H (**Fig. 1c-d**)[13]. Thus, the amorphous layer coating on the particle could be attributed to ammonium bicarbonate (proton-rich shell). The probable reaction route could be pictured as the following invertible equation:

$$NH_4HCO_3 \rightleftharpoons NH_3 + H_2O + CO_2$$

During the heating process, the ammonium bicarbonate decomposed into NH_3, CO_2 and

H_2O gas, and then uniformly regenerated as ammonium bicarbonate on the particle surface by chemical vapor deposition during the cooling process[14]. Notably, proton is homogeneously introduced on the SN92-H particle via ammonium bicarbonate coating and then would be in situ converted to sub-nano F-&P-maskant (discussed later). Laboratory XRD measurements (λ_{Cu} = 1.54059 Å) and the correlated Rietveld refinement results further proved that with the proton-rich shell, the SN92-H kept the same space group of hexagonal $R\bar{3}$m with SN92. According to the details of Rietveld refinement (**Table. S2-3**), the calculated lattice parameters of SN92-H are a = b = 2.875(3) Å and c = 14.185(6) Å, which are near the same as that of SN92 (a = b = 2.875(2) Å and c = 14.185(3) Å), illustrating the negligible bulk change after the coating process. Overall, a uniform surficial enriched proton shell was successfully introduced on SN92 through chemical vapor deposition of proton-carrier ammonium bicarbonate.

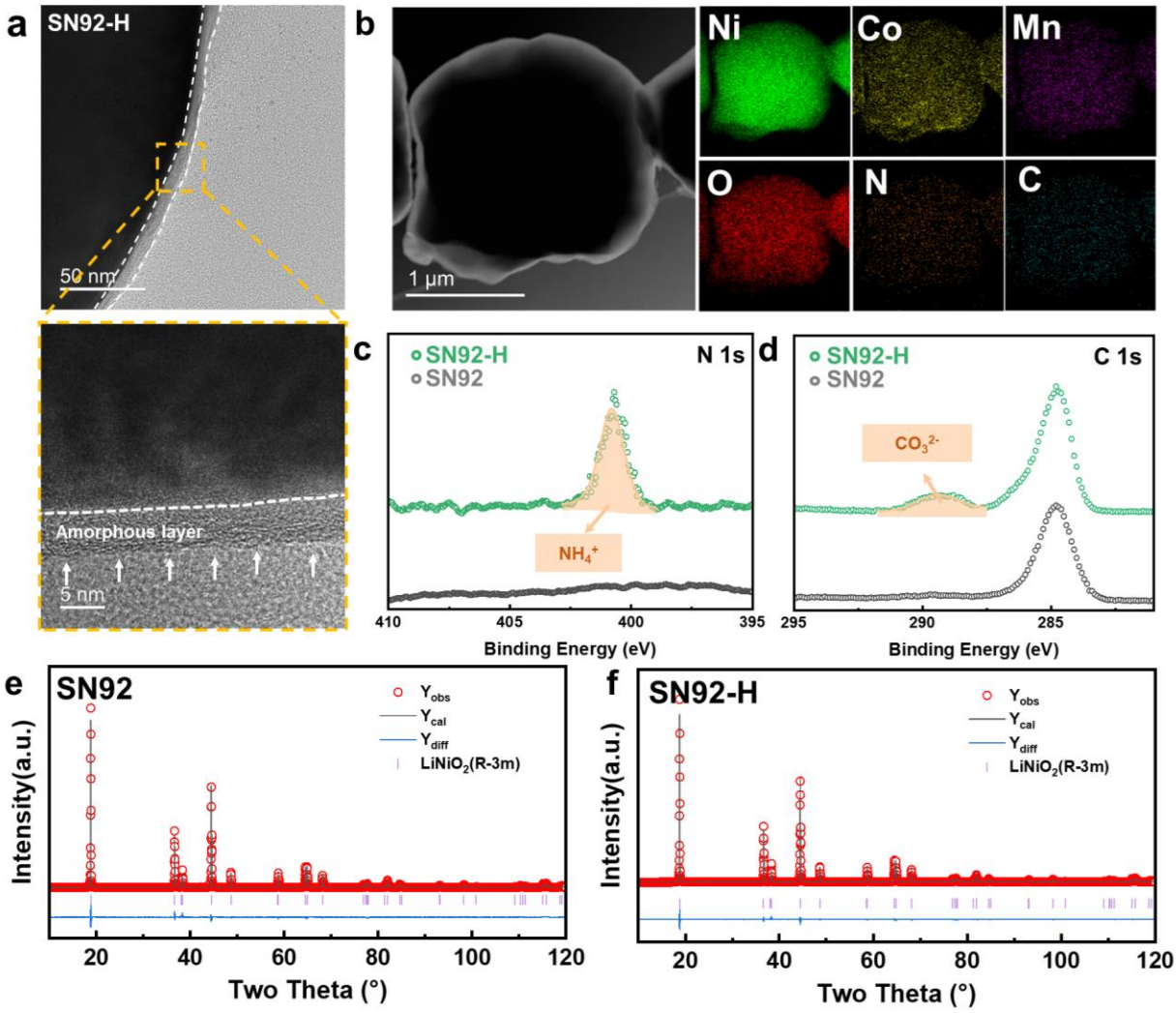

Figure 1: **Construction of proton-rich shell**. (a)The high-resolution TEM image of SN92-H. (b)The TEM-EDS mapping of SN92-H with even distribution of Ni, Mn, Co, N and O elements. (c-d) The XPS spectra of N 1s (c) and C 1s (d) for SN92 and SN92-H. (e-f) Powder XRD pattern and Rietveld refinement plot of SN92 (e) and SN92-H (f), respectively.

In situ electrochemical conversion of the proton-rich shell

As expected, the homogeneous proton-rich shell would react and transform to compact

sub-nano F-&P-maskant. Through combination of operando FT-IR and in situ UV, the in-situ conversion process was carefully examined. According to the operando FT-IR of SN92 (**Fig. 2a)**, a clear variation of electrolyte could be pictured along with the voltage upward and depth of electrochemical reaction. The ethylene carbonate (EC) at 1800 cm^{-1} , dimethyl carbonate (DMC) at 1736 cm^{-1} and $LiPF_6$ at 843 cm^{-1} [15] gradually decreased, whereas correlated side product of dehydrogenated EC (de-H EC) at 1827 cm^{-1}, VC (also regarded as de-2H EC) at 1830 cm^{-1} and dehydrogenated oligomers with EC-like rings at 1763 cm^{-1} gradually increased, which was consistent with previous researches[16]. In sharp contrast with the SN92, the operando FT-IR pattern (**Fig. 2b**) of SN92-H performed no obvious signal changes of both electrolyte and side product until the cell was charged up to ~4 V. A logical explanation is that the ammonium bicarbonate coating layer blocks the reaction between the electrolyte and active material when the voltage is below 4 V. Upon charging to the decomposition voltage of carbonate at about 4 V[17], the ammonium bicarbonate was decomposed and the corresponding signals of additive and side products were detected by FI-IR. To further demonstrate the blocking effect of ammonium bicarbonate, a coin-type cell with ammonium bicarbonate cathode and Li metal anode was examined in the same electrolyte and the corresponding electrochemical profile (**Fig. S5**) showed a typical decomposition plateau at about 4 V, which was consistent with the operando FT-IR. The SN92-H exhibits more $LiPF_6$ decomposition but less organic electrolyte decomposition at 4.4 V (**Fig. S6a-b**). We speculated that the interfacial proton from the decomposed proton-rich shell (ammonium bicarbonate) can react with the $LiPF_6$ and then hinder the side

reaction with the organic electrolyte with the assistance of the correlated product (the sub-nano F-&P- maskant as proved latter). Moreover, in situ UV (**Fig. 2c-d** and **Fig. S7**) was further conducted to monitor the chemical reactions between the particle and electrolyte. Within the wavelength range of 280 nm to 330 nm, a broad peak non-selectively appeared and gradually grew for Ni-based SN92, Co-based $LiCoO_2$ and Mn-based $LiMn_2O_4$ and therefore could be regarded as the decomposition products of electrolyte (**Fig. S8**)[18]. The decomposition products progressively increase for SN92 with voltage upward, whereas the correlated signals for SN92-H appear only after charging to about 4.0 V, consistent with operando FT-IR. Interestingly, a distinctive peak at the 394 nm of Ni ions dissolution[19] appears simultaneously with the electrolyte decomposition for the SN92-H as the SN92 does not perform. A logical explanation can be demonstrated as that the proton reacts with the $LiPF_6$ to generate the HF. The Lewis acid HF would undoubtedly attack the crystal and result in the Ni ions dissolution, which further proves the existence and the conversion of the proton on the interface. Similar to the FT-IR result, the decomposition signal intensity of the organic components for SN92-H at 4.3 V in UV pattern (**Fig. S9**), is significantly lower than that of SN92. The XPS spectra of C 1s (**Fig. S10**) additionally support the findings as the SN92 exhibits a higher ratio of OCO_2. All in all, the decomposition and resulting invalidation of the proton-rich shell in the first cycle is convinced, which means the functional components during the long-term cycling is others (most likely the compact sub-nano F-&P-maskant as characterized later).

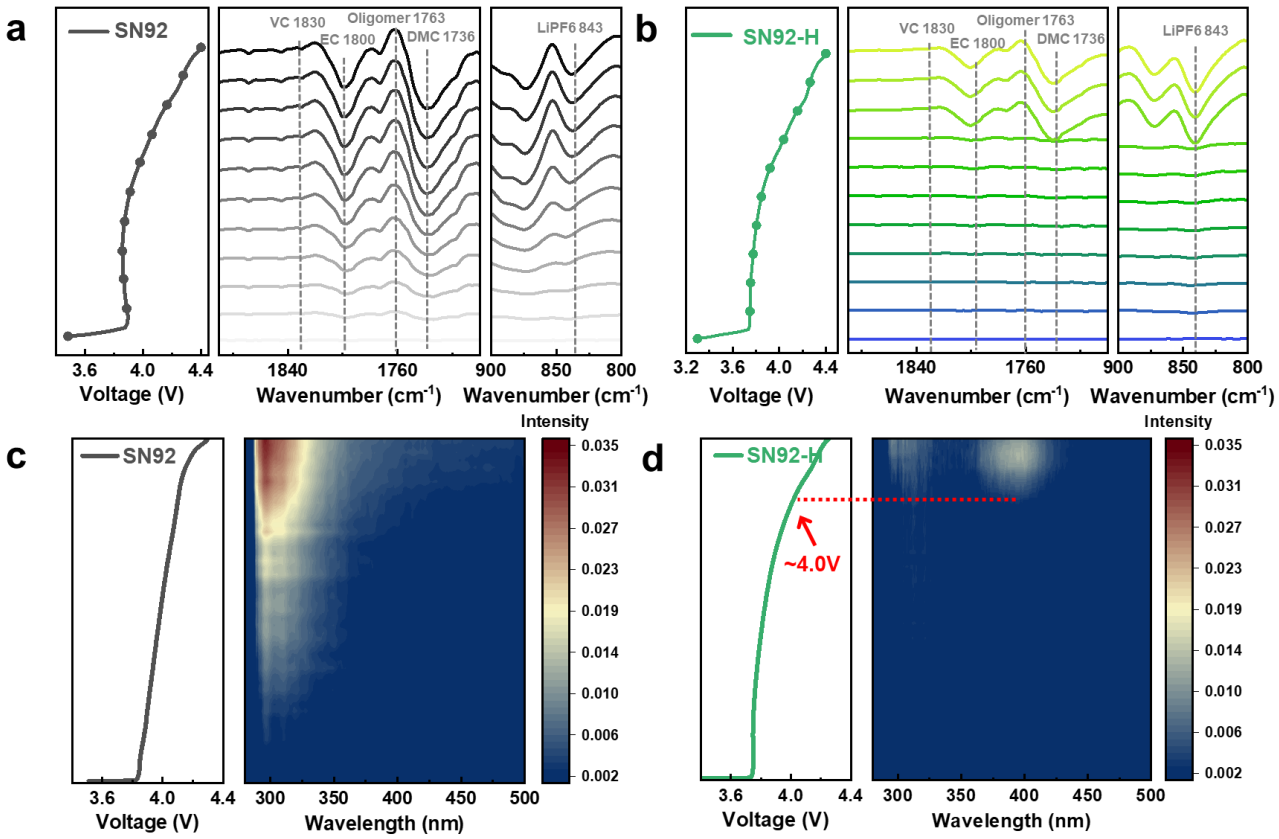

Figure 2: **Characterizations of the cathode/electrolyte interface reaction in 1st cycle.** (a-b) Operando FT-IR difference spectra in C=O and P-F stretching region on SN92 (a) and SN92-H (b) surface during charging to 4.4 V at the initial cycle. Inserted dashed lines depict the finger peak of different compositions: VC (1830 cm^{-1}), EC (1800 cm^{-1}), Oligomer (1763 cm^{-1}), DMC (1736 cm^{-1}), $LiPF_6$ (843 cm^{-1}). (c-d) In situ UV spectra of electrolyte within SN92 (c) and SN92-H (d) half cell during charging to 4.3 V at the first cycle.

To further demonstrate that the converted interlayer of SN92-H consists of LiF and Li_3PO_4 sub-nano particle after the first cycle, cryo-TEM, ToF-SIMs and XPS were employed to monitor the composition around the surface area. With the visualization of the maskant

component from cryo-TEM (**Fig. 3a**), a compact (~2 nm) maskant built up by sub-nano crystals can be observed. The regions outlined in purple and pink are identified via HRTEM to ultrasmall Li_3PO_4 and LiF particle with sub-nano thickness, respectively. In contrast, the reacted interlayer on cycled SN92 displays an island-like distribution with non-uniform thickness, which is widely recognized as providing limited protection during subsequent cycling (**Fig. S11**). Further surface structure is shown in **Fig. 3b** and **Fig. S12**, a clear and uniform rock salt layer, ranging from 2 to 4 nm, was observed on the surface of cycled SN92-H, which may due to the electrophilic attack from Lewis acid HF during the proton-rich shell conversion process [20], whereas the rock salt regions for SN92 are island-like. Raman spectra (**Fig. S13**) further prove that the surface layered structure was converted to NiO and CoO structure for SN92-H after the first cycle. Moreover, based on the result of XPS (**Fig. 3c-d**), it is clear that SN92-H exhibited a higher concentration of LiF and Li_3PO_4 compared to the SN92. A similar phenomenon can also be observed from the ToF-SIMs (**Fig. 3e**) as the SN92-H exhibits higher contents of LiF_2^- and PO_2^- fragments than SN92. Moreover, the chemical distribution map (**Fig. 3f-g** and **Fig. S14**) clearly illustrates the LiF_2^- and PO_2^- components are uniformly wrapped on SN92-H, while they are island-like distributed on SN92. Correspondingly, the normalized depth profile for SN92-H (**Fig. 3h**) also shows that both LiF_2^- and PO_2^- fragments stabilize at a constant value with an etching time of 50s. In sharp contrast, the normalized depth profile of LiF_2^- and PO_2^- fragments for SN92 (**Fig. S15**) reached a stable value at the etching time of 25s. All these results reveal that due to the presence of proton-rich shell, the SN92-H possesses thicker and more

uniform LiF and Li_3PO_4 sub-nano particles on its surface after the first electrochemical cycle compared to the SN92, indicating the protective maskant was successfully constructed on the surface of SN-92-H. In the electrolyte, the only component containing F and P elements is $LiPF_6$. Based on the above results, one can conclude that the abruptly produced local high-concentration proton by decomposition of proton-rich shell was immediately captured by $LiPF_6$ and nucleated to LiF and Li_3PO_4 sub-nano particles (**Fig. 3i**)[11c]. The spatial distribution of the mechanical property of modulus was acquired from atomic force microscopy (AFM, **Fig. S16**)[21]. The modulus was more homogeneous for SN92-H after one cycle, compared to the unevenly distributed modulus of SN92. In addition, the thermal stability of the samples was examined by differential scanning calorimetry (DSC) characterization on the full charged state (4.4V). Compared to SN92, SN-92-H exhibits higher thermal stability as the exothermic reaction peak shifted toward a higher temperature by 10 ℃ and the heat release decreased by 114.7 J g^{-1}(**Fig. S17**). In general, the uniform proton-rich shell is transformed into homogeneous and compact maskant with a high ratio of LiF and Li_3PO_4 sub-nano particles, which are expected to hinder the side reactions between the SN92 particle and electrolyte in the subsequent cycles.

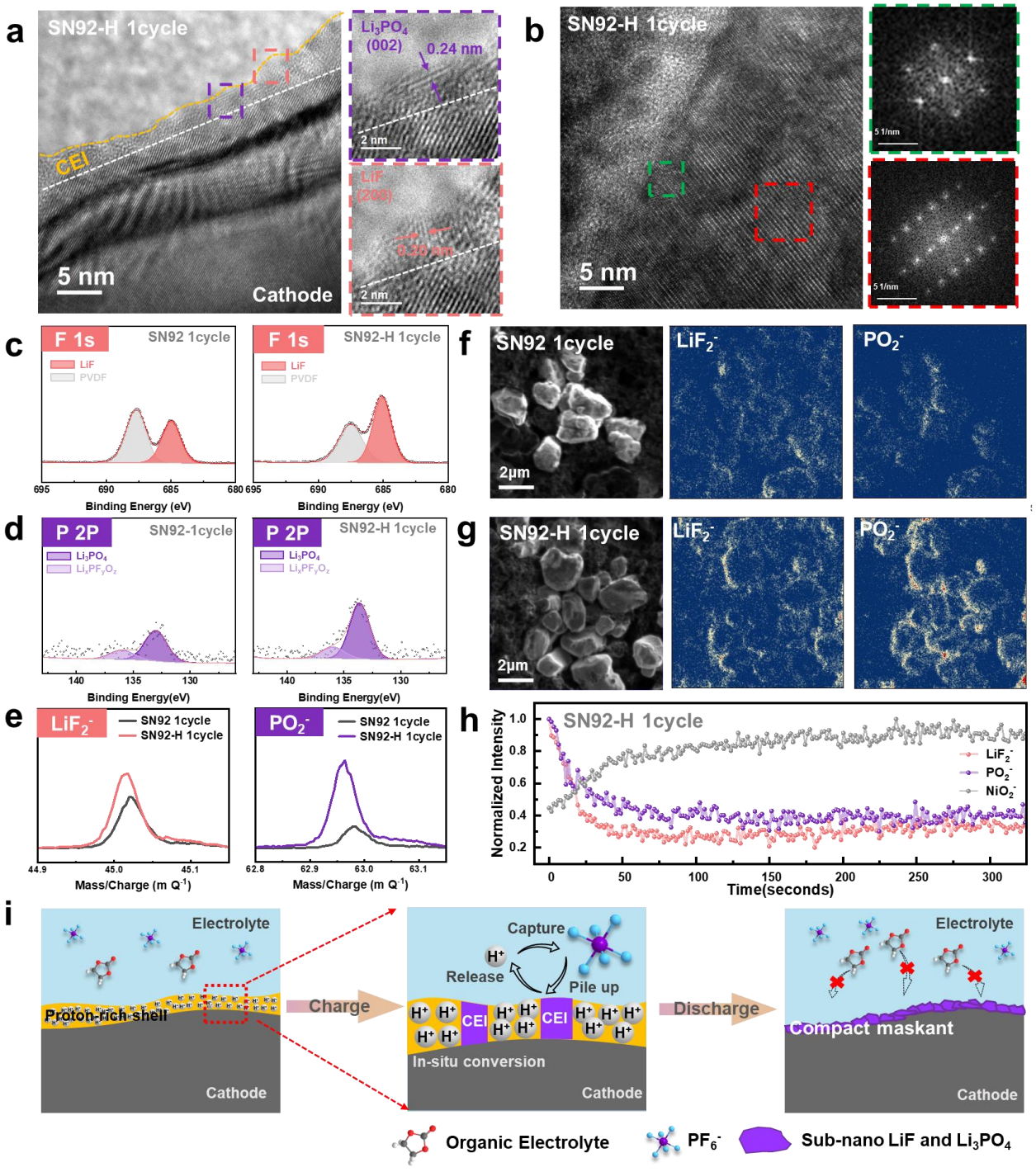

Figure 3: **Morphology and composition characterization of the maskant.** (a) The cryo-TEM images of SN92-H. (b) The high-resolution TEM images of the SN92-H and the corresponding FFT among different areas. (c-d) The XPS spectra with the same intensity

scale of F 1s (c) and P 2p (d) for SN92 and SN92-H. (e) TOF-SIMS spectra of LiF_2^- (left) and PO_2^- (right) on SN92 and SN92-H. (f-g) Chemical mapping of LiF_2^- and PO_2^- for the electrode of SN92 (f) and SN92-H (g) with the same intensity bar. (h) Normalized depth profiling of several secondary ion fragments of interest for SN92-H. (i) Schematics of the in situ conversion of the interfacial enriched proton to the sub-nano LiF- and Li_3PO_4-maskant.

Electrochemical performance

The effect of the sub-nano F-&P-maskant originating from the proton-rich shell and optimal synthesis condition was evaluated by electrochemical test (**Fig. S18**). As presented in **Fig. 4a**, both SN92 and SN92-H behaved the similar initial electrochemical profiles and delivered nearly the same capacity of ~220 mAh g^{-1} at 0.1 C (1 C= 200 mA g^{-1}) within the voltage range of 2.75-4.5 V (versus Li/Li^+), which demonstrates that the in situ converted LiF and Li_3PO_4 sub-nano particles provide Li^+ transports channel and do not result in energy density loss as general coating does[4a, 22]. After 100 cycles under 4.5 V cut-off voltage at 0.5 C (**Fig. 4b** and **Fig. S19a-b**), the SN92-H still maintained 186.6 mAh g^{-1} with a capacity retention of 95% (versus the initial capacity of 198.0 mAh g^{-1}). Whereas, the SN92 only delivered 172.9 mAh g^{-1} with a capacity retention of 87%. The corresponding differential capacity (dQ dV^{-1}) profile during cycling was displayed in **Fig. 4c-d**. It was obvious that both SN92 and SN92-H suffered a series of phase transitions, including hexagonal 1 to monoclinic (H1-M), to hexagonal 2 (M-H2), to hexagonal 3 (H2-

H3) during the charging process, and then underwent the reverse sequence during discharging[23]. The peak corresponding to the H2-H3 for SN92 gradually decreased during cycling, whereas that of SN92-H performed negligible change, illustrating the reversible H2-H3 transition with the help of the proton-converted sub-nano F-&P-maskant. Besides, H3-H2 transition peak of SN92 continuously shifted toward the lower voltage during cycling depicting gradually increased polarization, which was inhibited in SN92-H. After 120 cycles at 1 C (**Fig. 4e** and **Fig. S19c-d**), SN92-H still exhibits a capacity retention of 91% much higher than 78% for SN92. Particularly, both the SN92-H and SN92 deliver better capacity retention at a slow rate of Li extraction even at a higher cutoff voltage of 4.5 V, which may be due to the slow migration rate of Li ions in high nickel single crystal[24]. In order to evaluate the potential for commercial application, full cells with the sample as cathode and graphite as anode were examined within the voltage range of 2.65-4.3 V at 1 C (**Fig. 4f**). The SN92 and SN92-H full cells delivered near the same capacity with 209.8 mA g^{-1}, 209.2 mA g^{-1} at 0.1 C, and 180.2 mA g^{-1}, 180.1 mA g^{-1} at 1 C, respectively. The SN92-H full cell performed excellent long-term cycling stability with capacity retentions of 87% and 83% after 400 cycles and 800 cycles, respectively. In sharp contrast, the SN92 only kept 71% and 66% of the initial capacity after 400 cycles and 800 cycles, respectively. All in all, the in situ constructed sub-nano F-&P-maskant at the initial cycle significantly improved the long-term cycling stability of SN92-H.

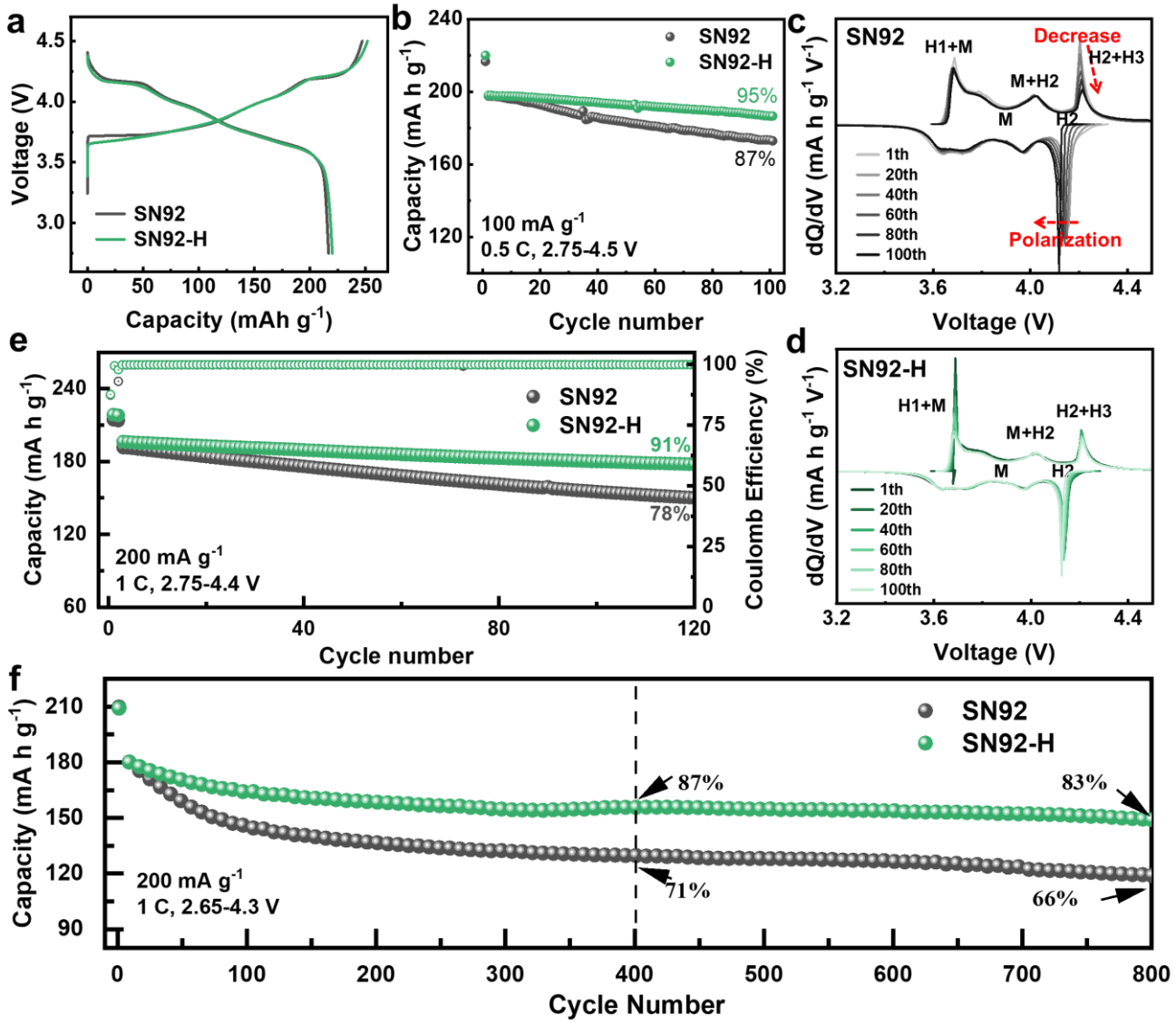

Figure 4: **Electrochemical performance**. (a) Charging and discharging curves of SN92 and SN92-H at the first cycle. (b) Cycling stability for SN92 and SN92-H half cells within the voltage range of 2.75-4.5 V at 0.5 C. (c-d) Corresponding dQ dV^{-1} profile of the 1^{st}, 20^{th}, 40^{th}, 60^{th}, 80^{th} and 100^{th} cycle for SN92 (c) and SN92-H (d). (e) Cycling stability for SN92 and SN92-H half cells within the voltage range of 2.75-4.4 V at 1 C. (f) Cycling performance of full cells with SN92 or SN92-H as cathode and graphite as anode within

the voltage range of 2.65-4.3 V at 1 C.

Enhanced surface stability by sub-nano F-&P-dense maskant

Continuous side reactions between the Ni-rich cathode and electrolyte during electrochemical cycling are detrimental to the battery lifetime. After 200 cycles at 1 C, the interfacial-relevant issues were further detected by the ToF-SIMs, XPS and EELS. As shown in ToF-SIMs patterns (**Fig. 5a-b**), the profiles of representative fragments reveal the distinct states of the two cathode-electrolyte interphase (CEI) films. For SN92, LiF_2^-, PO_2^-, C_2HO^- and C_6H^-, exhibited long-range distribution among the depth and remained at a constant value with a sputtering time of 500 s, demonstrating a thick CEI from serious interaction between cathode and electrolyte. In stark comparison, the intensity value of these fragments stabilized only after 200s for SN92-H. As shown in the 3D reconstruction patterns (right area of **Fig. 5a-b**), the LiF_2^-, PO_2^-, C_2HO^- and C_6H^- fragments of SN92-H gathered together near the surface area, whereas these fragments extended deep into the bulk due to the thick CEI of SN92, indicating a more compact and thinner maskant/CEI for SN92-H. The same tendency could also be seen in other fragments (C_2H^-, C_4H^- and $Li_2F_3^-$ (**Fig. S20** and **Fig. S21**)). Further characterization of the F 1s and P 2p XPS spectra without etching (**Fig. S22**) revealed that the long-term cycled SN92-H exhibited a higher concentration of LiF and Li_3PO_4 near the surface compared to SN92. Therefore, we could conclude that the proton-conversed LiF and Li_3PO_4 sub-nano particle maskant during the first cycle were densified and chemically stable, which persisted self-integrity and

contributed to the enhanced surface stability of SN92-H during long-term cycling. The O 1s and Ni 2p XPS spectra (**Fig. 5c** and **Fig. S23**) with increasing etching time were also conducted and revealed stronger peak signals of crystal oxygen and nickel element among all depths for SN92-H than SN92. These XPS results also indicated the thinner CEI for long-term cycled SN92-H. Furthermore, the HAADF-STEM and TEM-EELS (**Fig. 5d-e** and **Fig. S24**) were applied to examine the crystal oxygen loss and surface structure degradation by interfacial reaction. The HAADF-STEM image taken along the [100] zone axis of cycled SN92 clearly shows the irregularly shaped and thick rock salt phase, ranging from 3 to 12 nm on the surface, and with a large-scale mixed phase ($R\bar{3}$m layered and $Fm\bar{3}m$ rock salt from FFT image) in the internal area. In sharp contrast, cycled SN92-H exhibited a thinner and more uniform rock salt phase (~5 nm) on the surface and a nearly complete layered phase in the internal area, which can be attributed to the alleviated interfacial reaction due to the protection of the sub-nano F-&P-maskant[12d]. The EELS line scan spectra from surface to bulk depict a similar tendency, as cycled SN92-H showed a more prominent O pre-edge peak at 530 eV compared to cycled SN92, indicating less crystal oxygen loss of the former. A similar phenomenon is observed in the HRTEM images (**Fig. S25**), where SN92 shows extensive surficial distortion and the formation of a rock-salt phase along the (003) plane. In contrast, SN92-H maintains the structural integrity of the (003) plane even after long-term cycling. Overall, with the assistance of proton-converted compact sub-nano F-&P-maskant, the side reaction was significantly hindered in SN92-H. And consequently, an improvement was expected in the long-range

electrochemical cycle performance. Moreover, serious interfacial side reactions between cathode material and electrolyte always gave rise to the continuous dissolution of Ni ions from SN92 into the electrolyte. Thus, the inductively coupled plasma-mass spectrometry (ICP-OES) was performed to directly measure the concentration of dissolved Ni ions in electrolyte after 50 cycles among a voltage range of 2.75-4.3 V (**Fig. S26a**)[25]. It was noticed that the Ni ions concentration was 3.44 mg L^{-1} in the electrolyte of SN92 and significantly decreased to 2.42 mg L^{-1} for the SN92-H. The correlated 3D render of NiO_2^- in **Fig. S26b** pictures the consistent phenomenon as the SN92 exhibits decreased signals among the surface, illustrating the more serious Ni ions dissolution from the cathode particle compared to SN92-H. Particularly, although the SN92-H performed obvious Ni ions dissolution during the first cycle due to the Lewis acid HF attack, the SN92-H alleviated ion dissolution among the subsequent cycles under the assistance of the compact sub-nano F-&P-maskant. Additionally, SN92-H exhibit lower electrochemical impedance spectroscopy (EIS) resistance than SN92 after 200 cycles (**Fig. S27** and **Table. S4**). Based on these results, it is obvious that SN92-H performs the mitigated interfacial reaction and behaves thinner CEI than SN92 after long-term electrochemical cycling.

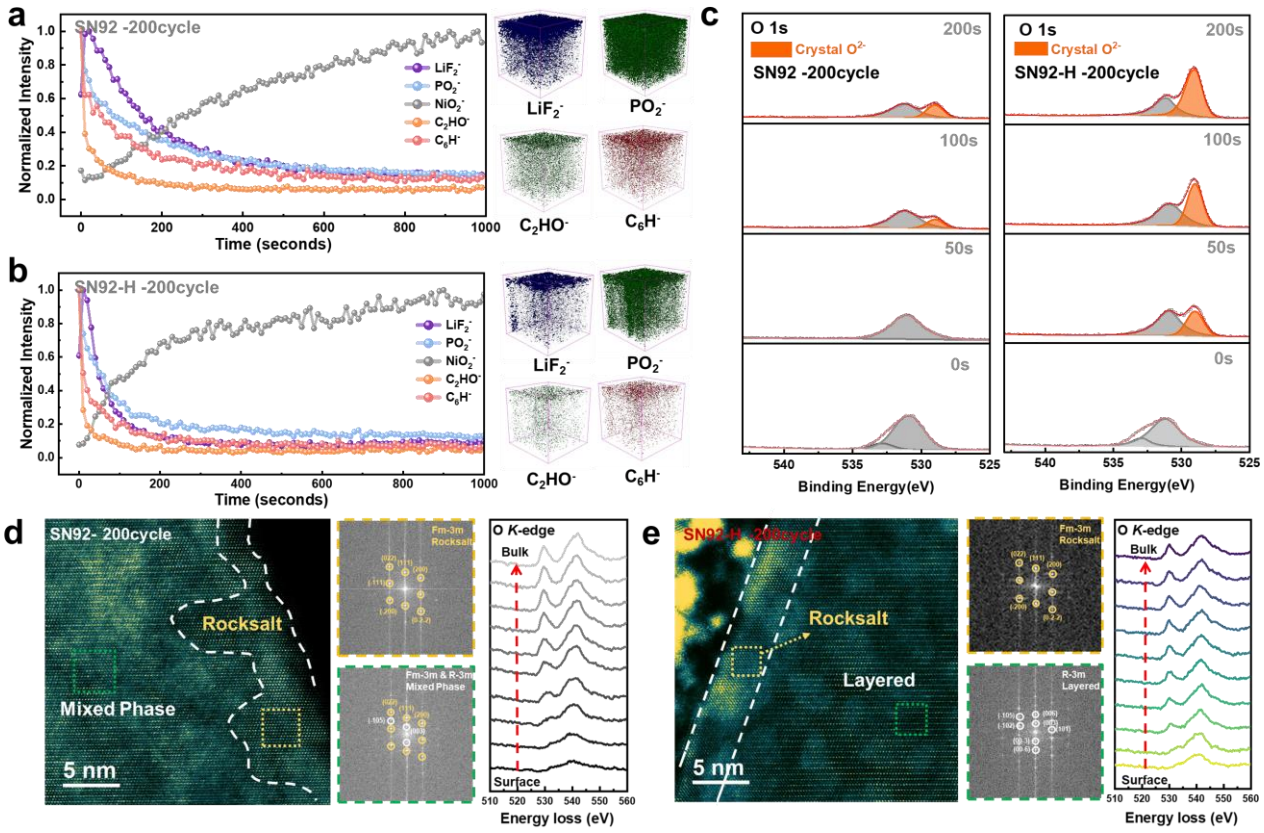

Figure 5: **Surface comparison after long-term electrochemical performance**. (a-b) ToF-SIMs depth profiles for SN92 (a) and SN92-H (b) of LiF_2^-, PO_2^-, C_2HO^-, C_6H^- and NiO_2^- fragments. The correlated 3D render of LiF_2^-, PO_2^-, C_2HO^- and C_6H^- were pictured in the right area. (c) The XPS spectra of O 1s with 0s, 50s, 100s and 200s (related with the depth of 0nm, 25nm, 50nm and 100nm, resepectively) etching for SN92 and SN92-H. (d-e) The HAADF-STEM image and correlated FFT patterns of the SN92 (d) and SN92-H (e) and corresponding EELS spectra of the oxygen K-edge from surface to bulk in the same area.

Discussion

The artificial proton-rich shell, compact maskant and surface stability

In the traditional lithium battery system using $LiPF_6$ as the lithium salt, a long-held perspective involves proton is the reaction with the $LiPF_6$ and resulted LiF and Li_3PO_4. In this work, we successfully achieved artificially surficial enriched proton on the nickel-rich single crystal (SN92-H) *via* ammonium bicarbonate shell as proton reservoir. Through the comprehension examination by operando FT-IR, in situ UV, XPS, ToF-SIMs, cryo-TEM and AFM, we could illustrate that the locally enriched proton from the decomposition of proton-rich shell would, in situ convert to LiF and Li_3PO_4 sub-nanoparticle dense maskant by reacting with $LiPF_6$ during the first cycle. While such investigations may not stray beyond common knowledge about the proton, distinctive results were revealed as SN92-H exhibited improved long-term cycling stability. Upon focusing on the CEI thickness and corresponding side reaction degrees analyzed by TOF-SIMs, SN92-H exhibited more significant $LiPF_6$ decomposition induced by the introduced proton during the first cycle. Excitingly, it showed an obvious alleviation of surface side reactions during the subsequent long-term cycling compared to SN92, consistent with its electrochemical performance. This unusual phenomenon prompted us to investigate the differential effects between artificial proton and natural proton, which we summarized as “local enrichment” and “compact”. For the SN92-H, taking advantage of uniformity of proton-rich shell, protons were locally enriched on the surface in spatial attribution. Additionally, performing as the nucleation site of inorganic product, the proton-rich shell was converted to sub-nano F-&P-

dense-maskant with high uniformity. In sharp contrast, SN92 exhibited an island-like arrangement of maskant (**Fig. 6**) as the natural proton distributes randomly in system, which failed to gather and transform to uniform and compact maskant. As a result, this in situ formed high-quality maskant significantly hindered the interaction between the cathode material and organic electrolyte during the subsequent cycling, improving SN92-H's surface stability, as proved by TOF-SIMs and TEM-EELS. Considering surface stability from this perspective, the critical factor can be attributed to proton local enrichment and resulting maskant compactness. Therefore, it's not surprising that SN92-H exhibited 95% capacity retention after 100 cycles within the voltage range of 2.75-4.5 V and excellent long-term cycling retention of 83% after 800 cycles with graphite as the anode. In summary, these results clearly demonstrate that the surficial enriched proton using uniformly coated ammonium bicarbonate as a carrier is an effective strategy to defend nickel-rich single crystal cathodes against side reactions. Moreover, this inspiring finding highlights the coating layer reconstruction strategy and the critical role of surficial enrichment and compactness in proton utilization, potentially accelerating the commercial application of nickel-rich single crystals.

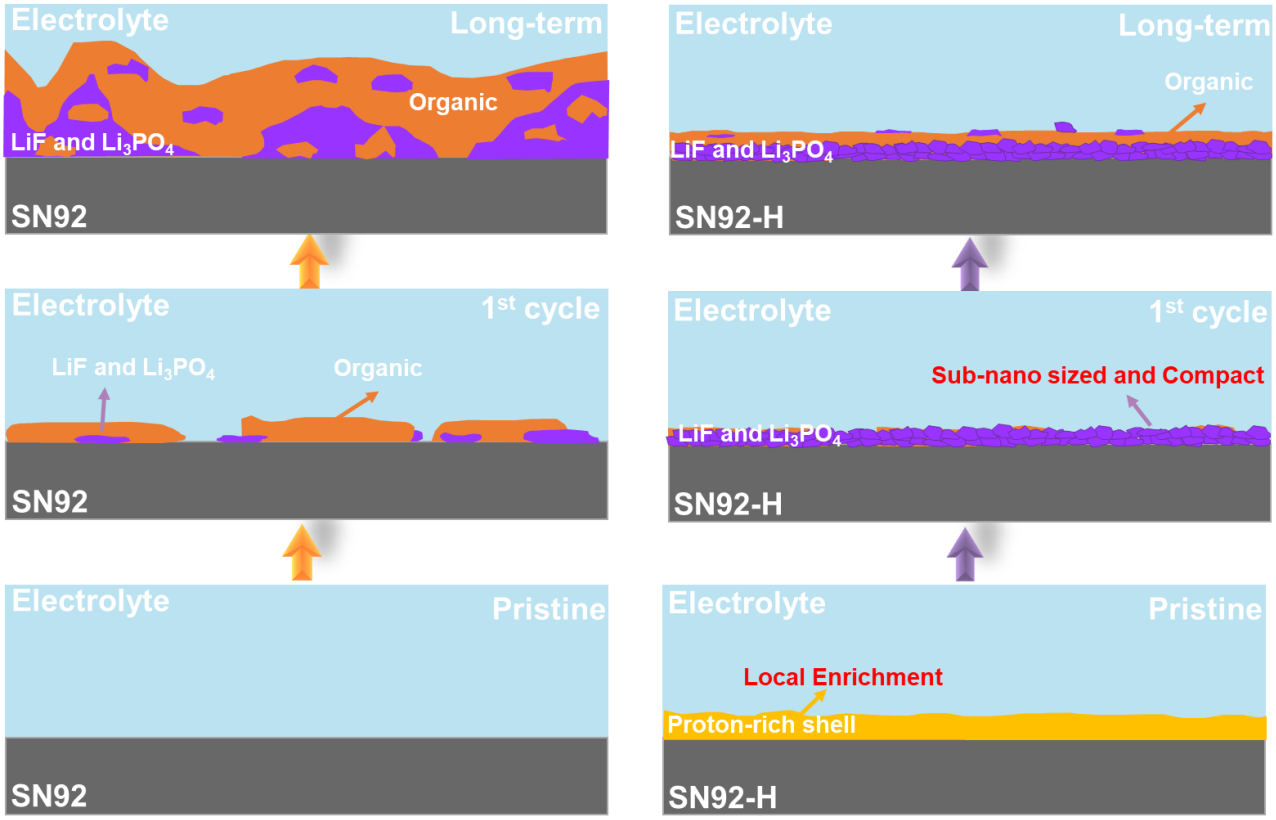

Figure 6: **Schematic illustration of the difference between the SN92 and SN92-H interfacial components**. The purple area is the inorganic decomposition product from $LiPF_6$. The orange area is the organic side reaction produced by the electrolyte. Due to the compact LiF and Li_3PO_4 sub-nano particle dense maskant from the proton-rich shell, the decomposition of the $LiPF_6$ and electrolyte is hindered during the long-term cycling. Whereas the island-like inorganic maskant cannot effectively protect the particle from the continuous attack of electrolyte, which results in thicker CEI for SN92.

Methods

Synthesis of the SN92-H

Commercial SN92 was mixed with varying weight ratios (0–2%) of ammonium bicarbonate using a mortar and pestle. The resulting mixture was transferred into a quartz tube, which was evacuated to approximately 1.0×10^{-3} Pa using a vacuum pump and sealed with an oxyhydrogen flame using a Partulab device. The sealed quartz tube was subjected to heat treatment at varying temperatures (100–300 °C) and holding times (5–15 minutes) at a heating rate of 10 °C min^{-1}. The optimal conditions for synthesizing SN92-H were determined to be 200 °C for 10 minutes with 1% ammonium bicarbonate.

Electronical measurement

The electrodes were prepared by blade-casting a slurry composed of 80% active materials, 10% poly(vinylidene difluoride) (PVDF) and 10% carbon black onto an aluminum foil and then drying at 80 °C in a vacuum for 12 h. The mass loading of the active materials was about 3 mg cm^{-2}. The 2032-type coin cells were assembled in an argon-filled glovebox with H_2O and O_2 <0.01 ppm. In the assembly process, the as-prepared electrode was used as the cathode, lithium metal or pre-lithiated graphite and Celgard 2316 served as the anode and separator, respectively. The solution of 1 mol L^{-1} $LiPF_6$ in ethylene carbonate/ethyl methyl carbonate (3/7 by weight) was employed as the electrolyte. Galvanostatic charge-discharge testing was carried out using NEWARE MHWX-200. EIS test (100 kHz to 0.01 Hz) was employed by an electrochemical workstation 1470E CellTest (Solartron, The

United Kingdom).

Materials characterization

The HRTEM characterization was employed by using a JEM-3200FS (JEOL, Japan). The cryo-TEM characterization was employed using the same JEM-3200FS with Gatan side-entry cryo-transfer holder (Gatan model 910) at around -178 ℃. The SEM-EDS characterization was employed by using a ZEISS SUPRA® 55(Carl Zeiss, Germany). The powder X-ray diffraction characterizations of NCM powders were carried out using a D8 Disvoer (Bruker, Germany) and corresponding crystal refinement was using the GSASII software. The EELS characterizations of cycled NCM powders were conducted by the high angle annular dark field scanning TEM (JEM ARM300F, Japan). The ICP test were conducted by PE/Avio 220 Max (PerkinElmer, American). The XPS characterization were carried out by ESCALAB 250Xi (Thermo Fisher, American). The DSC test was employed by DSC1 (METTLER TOLEDO, Switzerland). The Raman characterization was tested by inVia™ (Renishaw, The United Kingdom).

Operando FT-IR

An operando FT-IR spectro-electrochemical cell was assembled in the same argon-filled glovebox as mentioned before. Comprised composite NCM/nickel foam current collector is the positive electrode and a lithium metal is the negative electrode, separated by the glass fiber (Whatman). Operando FT-IR was then conducted by NICOLET iS50 Frontier-Infrared Spectrometer (Thermos scientific, America) within voltage a range of 2.75-4.4 V

at a current density of 60 mA g^{-1}.

In situ UV

An in situ UV spectro-electrochemical cell was assembled in the same argon-filled glovebox as mentioned before. A comprised composite NCM/ aluminum foil current collector is the positive electrode and a lithium metal is the negative electrode, both of which are in contact with the wire. Then the electrode slices are transferred into a Cuvette, which was added by 100 μL electrolyte and sealed. The in situ UV was then conducted by Shimadzu UV3600 (Japan) and Neware CT-4008T (China) within the voltage range of 2.75-4.3 V at a current density of 40 mA g^{-1}.

ToF-SIMs characterization of cycled cathode

The cycled coin cells were disassembled in an Ar-filled glove box, and the cycled cathodes were washed with the fresh ethyl methyl carbonate solvent for 3 times to dissolve the residual electrolyte. After that, the information of CEI on the cycled cathodes was acquired from time-of-flight secondary-ion mass spectrometry (ULVAC-PHI nanoTOF II, Japan and TESCAN SOLARIS GMH).

AFM study of the cycled cathode

The coin cells, after the initial cycle, were disassembled and the inserted cathodes were then washed with the fresh ethyl methyl carbonate solvent for 3 times as mentioned before. In order to avoid the decomposition of the CEI, the modulus distribution of the individual

particle was conducted in an argon-filled glove box by the atomic force microscope (Bruker Dimension Icon with TUNA, Germany) under the peak force tapping mode. The collected data were analyzed and pictured as 2D and 3D images by using the software Nanoscope Analysis 2.0 (Bruker, Germany).

Reference

[1] a)Q. Xie, W. Li, A. Manthiram, *Chemistry of Materials* **2019**, 31, 938; b)S.-T. Myung, F. Maglia, K.-J. Park, C. S. Yoon, P. Lamp, S.-J. Kim, Y.-K. Sun, *ACS Energy Letters* **2017**, 2, 196; c)J. Lu, C. Xu, *Chem* **2020**, 6, 3165.

[2] a)C. Wang, R. Zhang, C. Siu, M. Ge, K. Kisslinger, Y. Shin, H. L. Xin, *Nano Lett* **2021**, 21, 9797; b)M. Cai, Y. Dong, M. Xie, W. Dong, C. Dong, P. Dai, H. Zhang, X. Wang, X. Sun, S. Zhang, M. Yoon, H. Xu, Y. Ge, J. Li, F. Huang, *Nature Energy* **2023**, 8, 159; c)T. Dong, S. Zhang, Z. Ren, L. Huang, G. Xu, T. Liu, S. Wang, G. Cui, *Advanced Science* **2024**, 11, 2305753; d)K. Kim, H. Ma, S. Park, N.-S. Choi, *ACS Energy Letters* **2020**, 5, 1537; e)J. Li, L. E. Downie, L. Ma, W. Qiu, J. R. Dahn, *Journal of The Electrochemical Society* **2015**, 162, A1401.

[3] F. Lin, I. M. Markus, D. Nordlund, T.-C. Weng, M. D. Asta, H. L. Xin, M. M. Doeff, *Nature Communications* **2014**, 5, 3529.

[4] a)X. Fan, X. Ou, W. Zhao, Y. Liu, B. Zhang, J. Zhang, L. Zou, L. Seidl, Y. Li, G. Hu, C. Battaglia, Y. Yang, *Nat Commun* **2021**, 12, 5320; b)F. Wu, N. Liu, L. Chen, Y. Su, G. Tan, L. Bao, Q. Zhang, Y. Lu, J. Wang, S. Chen, J. Tan, *Nano Energy* **2019**, 59, 50.

[5] X. Fan, G. Hu, B. Zhang, X. Ou, J. Zhang, W. Zhao, H. Jia, L. Zou, P. Li, Y. Yang, *Nano Energy* **2020**, 70.

[6] a)I. Belharouak, C. Johnson, K. Amine, *Electrochemistry Communications* **2005**, 7, 983; b)Z. Chen, J. R. Dahn, *Journal of The Electrochemical Society* **2002**, 149, A1184; c)W. Liu, X. Li, D. Xiong, Y. Hao, J. Li, H. Kou, B. Yan, D. Li, S. Lu, A. Koo, K. Adair, X. Sun, *Nano Energy* **2018**, 44, 111; d)F. Schipper, H. Bouzaglo, M. Dixit, E. M. Erickson, T. Weigel, M. Talianker, J. Grinblat, L. Burstein, M. Schmidt, J. Lampert, C. Erk, B. Markovsky, D. T. Major, D. Aurbach, *Advanced Energy Materials* **2018**, 8, 1701682; e)J.-H. Shim, S. Lee, S. S. Park, *Chemistry of Materials* **2014**, 26, 2537; f)X. Xi, Y. Fan, Y. Liu, Z. Chen, J. Zou, S. Zhu, *Journal of Alloys and Compounds* **2021**, 872, 159664.

[7] G. Lu, Q. Qiao, M. Zhang, J. Zhang, S. Li, C. Jin, H. Yuan, Z. Ju, R. Huang, Y. Liu, J. Luo, Y. Wang, G. Zhou, X. Tao, J. Nai, *Science Advances*, 10, eado7348.

[8] H. H. Sun, H.-H. Ryu, U.-H. Kim, J. A. Weeks, A. Heller, Y.-K. Sun, C. B. Mullins, *ACS Energy Letters* **2020**, 5, 1136.

[9] Z. Chen, Y. Qin, K. Amine, Y. K. Sun, *Journal of Materials Chemistry* **2010**, 20, 7606.

[10] H. Ren, J. Hu, H. Ji, Y. Huang, W. Zhao, W. Huang, X. Wang, H. Yi, Y. Song, J. Liu, T. Liu, M. Liu, Q. Zhao, F. Pan, *Advanced Materials* **2024**, 36, 2408875.

[11] a)S. F. Lux, I. T. Lucas, E. Pollak, S. Passerini, M. Winter, R. Kostecki, *Electrochemistry Communications* **2012**, 14, 47; b)Z. Chen, Y. Ren, A. N. Jansen, C.-k. Lin, W. Weng, K. Amine, *Nature Communications* **2013**, 4, 1513; c)C. Bolli, A. Guéguen, M. A. Mendez, E. J. Berg, *Chemistry of Materials* **2019**, 31, 1258.

[12] a)J. Tan, J. Matz, P. Dong, J. Shen, M. Ye, *Advanced Energy Materials* **2021**, 11, 2100046; b)S. Tan, Z. Shadike,

J. Li, X. Wang, Y. Yang, R. Lin, A. Cresce, J. Hu, A. Hunt, I. Waluyo, L. Ma, F. Monaco, P. Cloetens, J. Xiao, Y. Liu, X.-Q. Yang, K. Xu, E. Hu, *Nature Energy* **2022**, 7, 484; c)H. Chen, L. Xiao, H. Chen, Y. Zhu, K. Xiang, H. Liao, *Electrochimica Acta* **2020**, 344, 136142; d)C. Wang, L. Han, R. Zhang, H. Cheng, L. Mu, K. Kisslinger, P. Zou, Y. Ren, P. Cao, F. Lin, H. L. Xin, *Matter* **2021**, 4, 2013; e)Y.-h. Luo, Q.-l. Pan, H.-x. Wei, Y.-d. Huang, L.-b. Tang, Z.-y. Wang, C. Yan, J. Mao, K.-h. Dai, Q. Wu, X.-h. Zhang, J.-c. Zheng, *Materials Today* **2023**, 69, 54; f)Y.-H. Luo, Q.-L. Pan, H.-X. Wei, Y.-D. Huang, P.-Y. Li, L.-B. Tang, Z.-Y. Wang, C. Yan, J. Mao, K.-H. Dai, Q. Wu, X.-H. Zhang, J.-C. Zheng, *eScience* **2024**, 4, 100229.

[13] a)J. Zheng, P. Yan, D. Mei, M. H. Engelhard, S. S. Cartmell, B. J. Polzin, C. Wang, J.-G. Zhang, W. Xu, *Advanced Energy Materials* **2016**, 6, 1502151; b)W. Wu, Y. Bo, D. Li, Y. Liang, J. Zhang, M. Cao, R. Guo, Z. Zhu, L. Ci, M. Li, J. Zhang, *Nano-Micro Letters* **2022**, 14, 44; c)S. Hiromoto, K. Kano, Y. Suzuki, K. Asami, A. Chiba, T. Hanawa, *MATERIALS TRANSACTIONS* **2005**, 46, 1627.

[14] S. Lobe, A. Bauer, S. Uhlenbruck, D. Fattakhova-Rohlfing, *Advanced Science* **2021**, 8, 2002044.

[15] D. J. Xiong, M. Bauer, L. D. Ellis, T. Hynes, S. Hyatt, D. S. Hall, J. R. Dahn, *Journal of The Electrochemical Society* **2018**, 165, A126.

[16] Y. Zhang, Y. Katayama, R. Tatara, L. Giordano, Y. Yu, D. Fraggedakis, J. G. Sun, F. Maglia, R. Jung, M. Z. Bazant, Y. Shao-Horn, *Energy & Environmental Science* **2020**, 13, 183.

[17] M. Sathiya, J. Thomas, D. Batuk, V. Pimenta, R. Gopalan, J.-M. Tarascon, *Chemistry of Materials* **2017**, 29, 5948.

[18] a)J. Li, W. Yao, Y. S. Meng, Y. Yang, *The Journal of Physical Chemistry C* **2008**, 112, 12550; b)G. Bouteau, A. N. Van-Nhien, M. Sliwa, N. Sergent, J.-C. Lepretre, G. Gachot, I. Sagaidak, F. Sauvage, *Scientific Reports* **2019**, 9, 135.

[19] M. Malik, K. H. Chan, G. Azimi, *RSC Advances* **2021**, 11, 28014.

[20] a)A. Tornheim, S. Sharifi-Asl, J. C. Garcia, J. Bareño, H. Iddir, R. Shahbazian-Yassar, Z. Zhang, *Nano Energy* **2019**, 55, 216; b)L. Giordano, P. Karayaylali, Y. Yu, Y. Katayama, F. Maglia, S. Lux, Y. Shao-Horn, *The Journal of Physical Chemistry Letters* **2017**, 8, 3881; c)H. Yaghoobnejad Asl, A. Manthiram, *Journal of the American Chemical Society* **2020**, 142, 21122.

[21] H. Sheng, X. H. Meng, D. D. Xiao, M. Fan, W. P. Chen, J. Wan, J. Tang, Y. G. Zou, F. Wang, R. Wen, J. L. Shi, Y. G. Guo, *Adv Mater* **2022**, 34, e2108947.

[22] X. Ou, T. Liu, W. Zhong, X. Fan, X. Guo, X. Huang, L. Cao, J. Hu, B. Zhang, Y. S. Chu, G. Hu, Z. Lin, M. Dahbi, J. Alami, K. Amine, C. Yang, J. Lu, *Nature Communications* **2022**, 13, 2319.

[23] a)T. Liu, L. Yu, J. Lu, T. Zhou, X. Huang, Z. Cai, A. Dai, J. Gim, Y. Ren, X. Xiao, M. V. Holt, Y. S. Chu, I. Arslan, J. Wen, K. Amine, *Nature Communications* **2021**, 12, 6024; b)X. Cheng, J. Zheng, J. Lu, Y. Li, P. Yan, Y. Zhang, *Nano Energy* **2019**, 62, 30.

[24] G.-M. Han, Y.-S. Kim, H.-H. Ryu, Y.-K. Sun, C. S. Yoon, *ACS Energy Letters* **2022**, 7, 2919.

[25] J. Peng, Y. Li, Z. Chen, G. Liang, S. Hu, T. Zhou, F. Zheng, Q. Pan, H. Wang, Q. Li, J. Liu, Z. Guo, *ACS Nano* **2021**, 15, 11607.

Acknowledgements

This work was financially supported by the Basic and Applied Basic Research Foundation of Guangdong Province (No. 2021B1515130002 and No. 2023A1515111131), International joint Research Center for Electric Vehicle Power Battery and Materials (No.2015B01015), Guangdong Key Laboratory of Design and calculation of New Energy Materials (No. 2017B030301013), Shenzhen Key Laboratory of New Energy Resources Genome Preparation and Testing (No. ZDSYS201707281026184).

Author contributions

H.X. and Y.L. contributed equally to this work. H.X., F.P., T.L. and X.T. conceived the ideas and designed all the experiments. F.P., T.L. and X.T. supervised the project. H.X. and Y.L. preformed the electrical characterization, in-situ characterization, and data processing. Y.H. performed the in-situ FT-IR test. Y.J. performed the AFM characterization. Z.X., X.C., H.W., K.A. and J.L. participated in the discussion of mechanism and provided personal insights. H.X. wrote the paper. All authors discussed the results and reviewed the paper.

Competing interests:

All authors declare no competing interests.

Additional information:

Correspondence and requests for materials should be addressed to Tongchao Liu,

Xinghua Tan, Feng Pan.

Supplementary information: The online version contains supplementary material available at ……

For Table of Contents

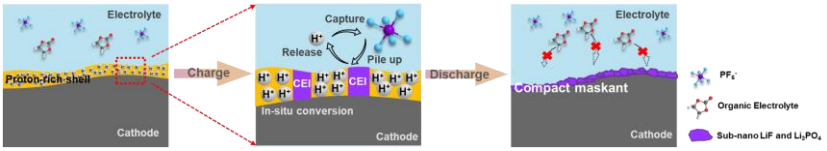

Table of Contents: In situ conversion of proton-rich shell to sub-nano particle dense maskant, which protects the single-crystal Ni-rich cathode from the attack of electrolyte in the long-term cycling and enables superhigh capacity retention of 83% after 800 cycles.

ToC figure is shown below as size of 110 mm × 20 mm (w × h).